JBC RESEARCH ARTICLE

Structural delineation and phase-dependent activation of the costimulatory CD27:CD70 complex

Received for publication, March 15, 2021, and in revised form, August 16, 2021 Published, Papers in Press, August 20, 2021,
https://doi.org/10.1016/j.jbc.2021.101102

Weifeng Liu[1,‡], Zachary Maben[2,‡], Carole Wang[1], Kevin C. Lindquist[1], Manqing Li[1], Vinayak Rayannavar[1], Ilsel Lopez Armenta[1], Andrew Nager[1], Edward Pascua[1], Pawel K. Dominik[1], David Oyen[1], Hui Wang[1], Rachel Carson Roach[1], Corey M. Allan[1], Lidia Mosyak[2,*], and Javier Chaparro-Riggers[1,*]

From the [1]Pfizer, Inc, La Jolla, California, USA; [2]Pfizer, Inc, Cambridge, Massachusetts, USA

Edited by Peter Cresswell

CD27 is a tumor necrosis factor (TNF) receptor, which stimulates lymphocytes and promotes their differentiation upon activation by TNF ligand CD70. Activation of the CD27 receptor provides a costimulatory signal to promote T cell, B cell, and NK cell activity to facilitate antitumor and anti-infection immunity. Aberrant increased and focused expression of CD70 on many tumor cells renders CD70 an attractive therapeutic target for direct tumor killing. However, despite their use as drug targets to treat cancers, the molecular basis and atomic details of CD27 and CD70 interaction remain elusive. Here we report the crystal structure of human CD27 in complex with human CD70. Analysis of our structure shows that CD70 adopts a classical TNF ligand homotrimeric assembly to engage CD27 receptors in a 3:3 stoichiometry. By combining structural and rational mutagenesis data with reported disease-correlated mutations, we identified the key amino acid residues of CD27 and CD70 that control this interaction. We also report increased potency for plate-bound CD70 constructs compared with solution-phase ligand in a functional activity to stimulate T-cells *in vitro*. These findings offer new mechanistic insight into this critical costimulatory interaction.

CD27 and CD70 are a receptor:ligand pair whose signaling activates and differentiates both T cells and B cells (1). CD27 is a receptor belonging to the TNF (tumor necrosis factor) receptor superfamily. CD27 expression has been observed in a majority of peripheral blood T cells with high CD27 surface expression detected on activated T cells (2–4). CD27 is also expressed on other lymphocytes including germinal center B cells, memory B cells, plasma B cells, and NK cells (3). The receptor CD27 can be shed from the cell surface through the activity of MMP-8 and the resulting soluble fragment has been shown to inhibit signaling, likely due to competition with intact CD27 for ligand (5, 6). The TNF ligand superfamily member CD70 is the only known ligand of CD27. CD70 exhibits transient surface expression on macrophages and mature DCs upon cell activation (7). CD70 expression is also detected on NK cells, B cells, and activated T cells (1).

The engagement of CD27 by CD70 induces signaling that affects many aspects of immune function. Downstream signaling depends on cytoplasmic segment of CD27 binding to TRAF (TNF receptor associated factor) signaling adaptors including TRAF2, TRAF3, and TRAF5 (8, 9). Both TRAF2 and TRAF5 can drive Janus kinase (JNK) activation, as well as canonical and alternative NF-κB activation, whereas TRAF3 inhibits the alternative NF-κB pathway (8–10). *In vitro* activation of CD27 by CD70 coincident with TCR engagement stimulates both human αβ and γδ T cell lineages to proliferate, secrete cytokines, and prolong survival (3). As an example of the importance of this costimulatory activity, patients with defective CD27:CD70 signaling caused by loss-of-function mutations are more susceptible to persistent EBV (Epstein–Barr virus) infections due to a paucity in memory B cells and EBV-specific T cells (both $CD4^+$ and $CD8^+$) (11, 12). These patients are consequently more likely to present with recurrent EBV-driven lymphoproliferative disorder and EBV-positive lymphoma (11–13).

The CD27:CD70 pathway does not only affect T cell activity as B cell activation and NK cell survival are also induced *via* reverse CD70 signaling upon CD27 receptor binding (3). CD70-mediated reverse signaling, which acts through PI3K and MEK transduction pathways (14), may explain the role of CD70 in tumor biology. CD70 expression is limited in normal tissues but is strongly expressed in many lymphomas and solid tumors including pancreatic, lung, renal and ovarian cancers (15, 16). The aberrant increase in CD70 expression on tumor cells correlates with increased proliferation and tumor survival (17, 18). Mouse models have shown that chronic CD70 expression promotes $CD8^+$ T cell exhaustion and impairs $CD8^+$ T cell differentiation, while clinical studies demonstrate that CD70 blockade decreases T_{reg} frequency and activity (15, 19, 20). In response to these observations, multiple antibodies and antibody drug conjugates targeting tumor-associated CD70 have been developed to directly deplete tumor cells and reverse CD70-mediated immune suppression (3).

Due to the immunostimulatory function of the CD27-CD70 signaling axis, augmentation of CD27 signaling has been identified as a potential therapeutic approach to promote

‡ Co-first authors: equal contribution.
* For correspondence: Lidia Mosyak, Lidia.Mosyak@pfizer.com; Javier Chaparro-Riggers, javier.chaparro-riggers@pfizer.com.

© 2021 THE AUTHORS. Published by Elsevier Inc on behalf of American Society for Biochemistry and Molecular Biology. This is an open access article under the CC BY-NC-ND license (http://creativecommons.org/licenses/by-nc-nd/4.0/).

T cell activation and improve antitumor efficacy. Transgenic constitutive expression of CD70 on B cells or dendritic cells has been shown to spontaneously convert naïve T cells into effector cells, promote T cell memory, and elicit more robust cytotoxicity against tumor in transgenic mouse models (21, 22). In an alternate strategy, administration of recombinant single-chain CD70-Fc fusion protein dramatically promoted antigen-specific T cell responses and demonstrated significant efficacy in two distinct tumor models (4, 23). Combination of CD27 agonism with PD-1/PD-L1 blockade preferentially activated Myc- and E2F1-dependent lymphocyte proliferative programs and protected against tumor challenges in mice (4, 24). As a result of efficacy in mouse models, agonistic antibodies targeting CD27 have been developed to treat cancer patients. Two different agonistic therapeutic antibodies (varlilumab and MK-5890) were reported to be well tolerated and exhibited clinical activity in patients with hematologic malignancies or solid tumors (25–27).

Herein we report the first crystal structure of human CD27:CD70 complex and demonstrate that CD27 and CD70 interact with 3:3 stoichiometry, in a manner similar to many other TNF receptor and ligand assemblies. Our CD27:CD70 structure also reveals key determinants involved in receptor:-ligand recognition and several unique structural features important for the selectivity of this system. Based on the structure of the CD27:CD70 complex, we designed and screened sets of CD27 and CD70 mutants to validate the key amino acids residues contributing to the binding interface. Finally, we also assessed the ability of recombinant CD70 constructs to activate T cells *in vitro*.

Results

CD70 exists as trimer in solution and interacts with glycosylated and deglycosylated monomeric CD27 with similar affinity

The full ectodomain of human CD27 contains three CRDs (cysteine-rich domains) and a stalk region with one cysteine (C185), which mediates receptor dimerization *in vivo* through intermolecular disulfide bond formation (8, 28). The human CD70 ectodomain contains a TNF homology domain and a stalk region. To minimize flexibility of CD27:CD70 protein complex for crystallization, we designed constructs encoding only a portion of the extracellular domains of these two binding partners (Fig. 1*A* and Fig. S1, *A* and *B*). To simplify the carbohydrate modification, we expressed both constructs in the presence of kifunensine and minimized the sugar modification by subsequent endoglycosidase (EndoH) digestion. Human CD27 protein could be readily deglycosylated with no significant aggregation (Fig. S2*B*). However, EndoH digestion of human CD70 protein resulted in aggregation (Fig. S2*A*). Therefore, we pursued structure determination using deglycosylated CD27 in complex with glycosylated CD70. SEC (size-exclusion chromatography) and CGE (capillary gel electrophoresis) indicated that deglycosylated CD27 and glycosylated CD70 were purified to homogeneity (Fig. 1*B* and Fig. S2, *A* and *B*). Molecular characterization by aSEC (analytical size-exclusion chromatography) suggested that CD70 forms a stable homotrimer and CD27 is a monomer in solution (Fig. 1*C*).

To assess the interaction of purified CD27 and CD70, we prepared mixtures of purified constructs in a 1:1 monomer molar ratio and assayed for complexation by monitoring the appearance of higher-molecular-weight species by aSEC. When CD27 and CD70 proteins were combined and incubated, we observed peaks corresponding to each individual component, indicating that the affinity between CD27 and CD70 does not support formation of a stable complex in solution (Fig. 1*C*). We therefore quantified the binding affinity between CD27 and CD70 by SPR (surface plasmon resonance). CD70 binds to glycosylated and deglycosylated CD27 with a K_D (equilibrium dissociation constant) of 134 ± 1 nM (average $k_a = 3.23 \times 10^4\ M^{-1}s^{-1}$; $k_d = 4.33 \times 10^{-3}\ s^{-1}$) and 118 ± 1 nM (average $k_a = 5.17 \times 10^4\ M^{-1}s^{-1}$; $k_d = 6.08 \times 10^{-3}\ s^{-1}$), respectively (Fig. 1, *D* and *E*). From the experimentally measured dissociation rate, the calculated half-life for these interactions is 2.67 and 1.90 min, respectively. This short half-life compared with the timescale of the SEC separation (more than 10 min) explains the lack of detectable complex by SEC. The binding affinities of glycosylated and deglycosylated CD27 to CD70 are similar, suggesting that the CD27 carbohydrate modifications do not significantly affect the interaction.

Human CD27:CD70 complex exhibits a 3:3 stoichiometry in the crystal

Crystallization of a complex between CD27 and CD70 was achieved by combining the individually purified components at a 1:1 monomer molar ratio and concentrating the sample prior to crystallization screens. We obtained crystals that diffracted to 2.69 Å with a space group of I222 (Table 1). The crystallographic asymmetric unit contains a single copy of the CD27:CD70 assembly composed of three CD27 monomers binding to one centrally located noncrystallographic CD70 homotrimer (Fig. 2*A* and Fig. S2*C*). Each CD27 monomer engages along the groove formed by two adjacent CD70 monomers. The three CD27 molecules in the asymmetric unit align very closely, with aligned C_α RMSDs ranging between 0.19 and 0.22 Å. Comparison of the structures of CD27 with previously determined CD27:Fab (fragment antigen binding) structures (PDB entries: 5Tl5, 5TLJ, 5TLK) shows minimal structural deviations within individual CRD domains. Moderate inter-CRD motion was observed when aligning the structures of CD27 from the CD27:CD70 complex and the CD27:Fab complex from the PDB entry 5Tl5, with a CRD1-CRD2 hinge difference of 3.4 degrees and a CRD2-CRD3 hinge difference of 10.7 degrees (Fig. 2*B*) (29). One N-linked glycan distant from the CD70-binding interface is observed on N95 residue within CRD2 of CD27 (Fig. 2*A* and Fig. S2, *C* and *H*), which is consistent with our SPR results indicating that CD27 glycans do not contribute significantly to the interaction with CD70.

The CD70 homotrimer resembles the classical TNF ligand trimeric assembly. The biologically active CD70 is formed by three protomers, with each protomer adopting a "jelly-roll" fold built around two β sheets (Fig. 2, *C* and *D*). Comparison of

ASBMB

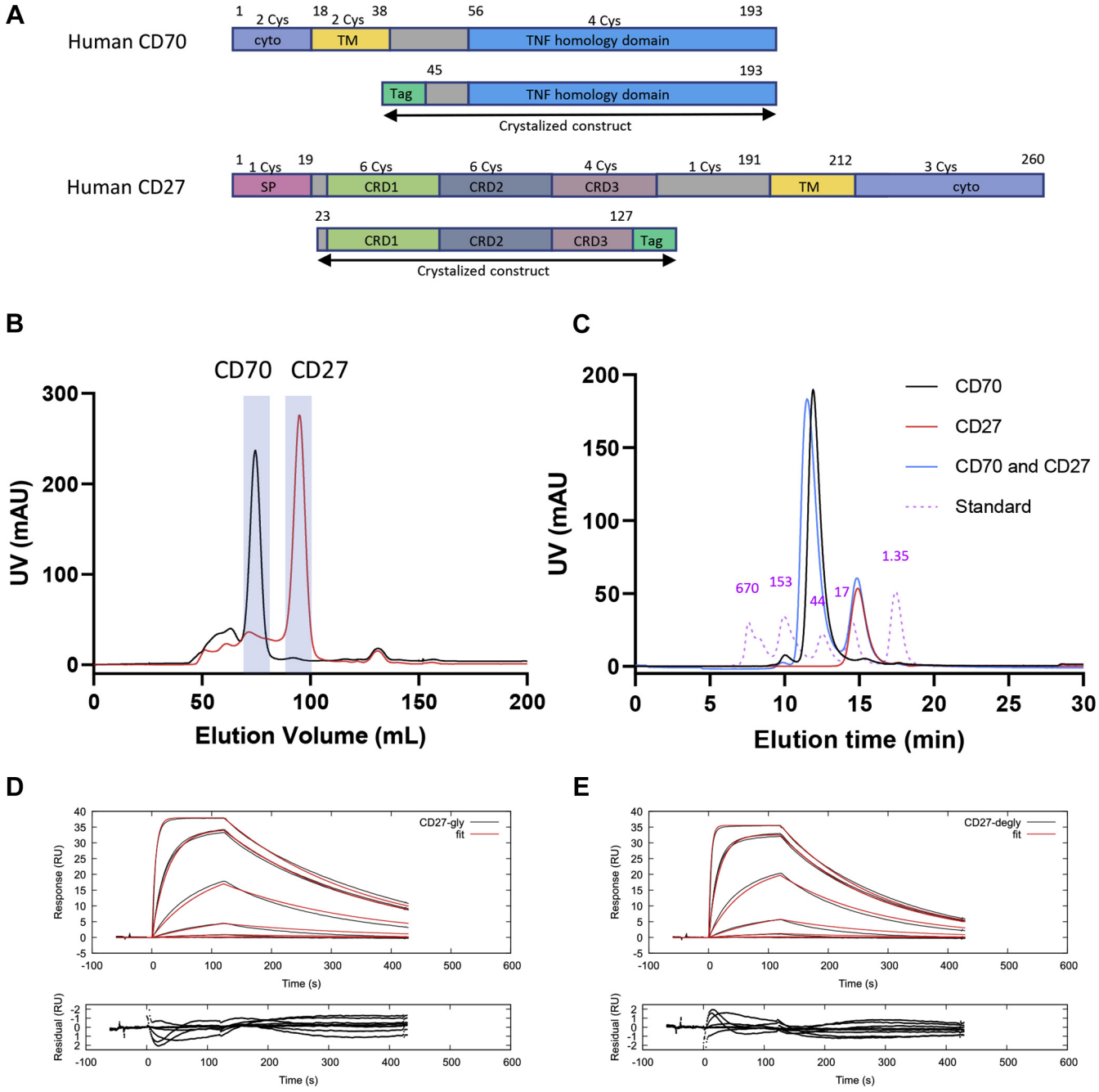

Figure 1. Design and characterization of human CD27 and CD70 for crystallization. *A*, design of the human CD27 and CD70 constructs for crystallization. *B*, SEC purification profiles of deglycosylated human CD27 (*red*) and glycosylated human CD70 (*black*) constructs for crystallization. The protein fractions used for biochemical assays and crystallization are highlighted in *blue*. *C*, analytical SEC of the purified human deglycosylated human CD27 (*red*) and glycosylated human CD70 (*black*), as well as the mixture of both proteins (*blue*). Molecular weight standard is shown in *magenta*. *D* and *E*, binding of glycosylated human CD27 (*D*) and deglycosylated human CD27 (*E*) to CD70-wt measured by surface plasmon resonance (SPR). *Upper panel* shows sensorgrams (*black*) and curve fit (*red*). *Lower panel* shows residuals from the curve fit. CD70 binds to glycosylated and deglycosylated CD27 with a K_D (equilibrium dissociation constant) of 134 ± 1 nM (average $k_a = 3.23 \times 10^4$ $M^{-1}s^{-1}$; $k_d = 4.33 \times 10^{-3}$ s^{-1}) and 118 ± 1 nM (average $k_a = 5.17 \times 10^4$ $M^{-1}s^{-1}$; $k_d = 6.08 \times 10^{-3}$ s^{-1}), respectively.

the CD70 homotrimer with representative TNF ligand structures demonstrates that CD70 adopts a "blooming flower" trimeric arrangement similar to OX40L (Fig. S3*C*). Electron density corresponding to N-linked glycan modifications extends from CD70 residues N63 and N170 on each protomer (Fig. 2*D* and Fig. S2, *C* and *E*–*G*). A region of density extending from O6 of the proximal N-acetylglucosamine moiety on residue N63 is consistent with a core fucosylation modification (Fig. 2*D* and Fig. S2, *E* and *F*). Superimposing the structure of CD70 protomer with a classical TNF ligand FasL shows a similar structural organization with an RMSD of 1.08 Å on 64 aligned C_α (Fig. S2*D*). Alignment of the scaffold β strands of CD70 and FasL shows even closer structural similarity with an RMSD of 0.64 Å on 35 aligned C_α (Fig. S2*D*). The most prominent structural differences between CD70 and FasL are present in the connecting loops between β strands.

Table 1
Crystallographic data collection and refinement statistics

Parameter	human CD27:CD70 complex
Data collection	
Space group	I222
Unit cell a, b, c (Å)	109.53, 113.63, 163.51
Unit cell α, β, γ (°)	90
Resolution (Å)	93.31–2.69 (2.98–2.69)
No. of total reflections	124,088
No. of unique reflections	18,602
R_{merge} (%)	10.5 (118)
R_{pim} (%)	4.4 (47.9)
Mean I/σ (I)	12.0 (1.7)
Spherical completeness (%)	64.9 (12.4)
Ellipsoidal completeness (%)	91.1 (55.4)
Multiplicity	6.7 (7.0)
$CC_{1/2}$	0.998 (0.727)
Wilson B-factor (Å^2)	54.4
Refinement	
Resolution (Å)	36.72–2.69 (2.85–2.69)
No. of reflections	18,587
R_{free} test set reflections	915 (4.92%)
R_{work}/R_{free} (%)	20.0/23.6
Mean B-factor (Å^2)	
All atoms	99.2
Protein	93.8
Ligand	193.9
Water	57.3
RMSD	
Bond length (Å)	0.008
Bond angle (°)	1.09
PDB entry	7KX0

Values in parentheses correspond to the highest-resolution shell.

A region of positive density along the CD70 trimer axis was identified. As mentioned above, the trimer is related by a threefold noncrystallographic symmetry; hence this additional density cannot be attributed to artifact of data processing. Based on the features of the density and the composition of the crystallization solution, a Tris molecule was modeled at this location (Fig. 2, *E*–*G*). This Tris molecule forms hydrogen bonds with each CD70 monomer, and it may be possible that the energetic stability of the trimer is strengthened by the contribution of these interactions. Further investigation into the effect of buffer components on CD70 homotrimer stability was warranted, and so differential scanning calorimetry (DSC) experiments were performed. The melting temperature of CD70 was found to increase when Tris was present, consistent with an energetic stabilization of the CD70 homotrimer upon binding of this small molecule (Fig. 2*H*). Interestingly, structures of TL1a (30) and mouse TNFα (31) also contain small molecules (glycerol, Tris, and isopropanol, respectively) bound along the ligand homotrimer axis. It may be of interest to assess activity or stability of these TNF family ligands in the presence and absence of these small molecules to ascertain the functional relevance, if any, of these hypothetical binding sites. As an example of the principle that ligand binding at the homotrimer axis may alter the stability of the macromolecular complex, a small-molecule SPD-304 was identified to bind a similar site in TNFα (32). SPD-304 binds to preformed TNFα trimer and induces a subunit rotation that displaces one TNFα monomer from the complex (32). Our structure provides a model that may be used to design a similar strategy to inhibit CD70 activity.

The unique disulfide bond of CD70

There are two pairs of intramolecular disulfide bonds observed in the structure of CD70. One disulfide bond is formed between residues C115 and C151 located on CD loop and EF loop, respectively (Fig. 2*D*). This disulfide bond is conserved among classical TNF ligands such as TNFα, LIGHT, TL1A, and FasL, *etc.* (Fig. S3*A*). The other disulfide bond, involving C168 on G β strand and C133 located on the DE loop, is unique to CD70 and was not observed in the previously determined TNF ligand structures (Fig. 2*D*). This disulfide bond is unusual in its position, which lies on the surface of the CD70 polypeptide (Fig. 2*D*) with 76.9% of the total surface area of the two side chain sulfur atoms exposed to solvent, except for the involvement of an additional posttranslational modification.

This disulfide bond is shielded by the N-linked glycan extending from N170, with the two N-acetylglucosamine moieties positioned directly over the disulfide bond (Fig. 2*D*). The disulfide-bonded cysteines and the observed shielding of N-linked glycosylation site are conserved in mouse CD70 (Fig. S3*A*), which is to be expected for structural features that are required for protein stability. Mutation of the glycosylation residues or the cysteines resulted in failure of protein expression and purification in Expi293 cells (data not shown). While the C133-C168 disulfide does not directly interact with CD27, it is likely that the conformational constraints imposed on the DE loop by the disulfide bond impact the CD70-CD27 interaction.

Binding interface between CD70 and CD27

Each CD27 molecule interacts with two CD70 monomers, forming an interface that buries a total of 2440 Å^2 of solvent accessible surface area from both CD27 and CD70. Two adjacent CD70 protomers contribute similar surface areas. For example, 653 Å^2 of surface area from CD27 chain F engages CD70 chain A and 707 Å^2 interacts with CD70 chain B (Fig. 3, *A* and *B*). Domains CRD2 and CRD3 of CD27 dominate the CD70-binding interface, with only a single residue from CRD1, F48, engaged in a van der Waals interaction with CD70 (Fig. 3*C*).

Examination of the recognition interface between CD27 and CD70 reveals atomic-level interactions contributing to the receptor:ligand complex. There are six ionic interactions observed between one CD27 receptor and its two interacting CD70 protomers (Fig. 3*C*). Residue E82 of CD27 contributes to two salt bridges: one with R83 from one CD70 protomer, the second with R138 from the adjacent CD70 protomer (Figs. 3*C* and 4, *B* and *C*). The other four salt bridges are formed by pairwise interactions between four CD27 acidic residues with four CD70 basic residue (Figs. 3*C* and 4, *B*–*D*). In addition to the ionic interactions, a network of 16 potential hydrogen bonds is observed within the recognition interface (Fig. 3*C*). Nine hydrogen bonds are formed between one CD27 (chain F) and one CD70 protomer (chain A), with the remaining seven hydrogen bonds formed between CD27 (chain F) and the adjacent CD70 protomer (chain B). All polar contacts

ASBMB

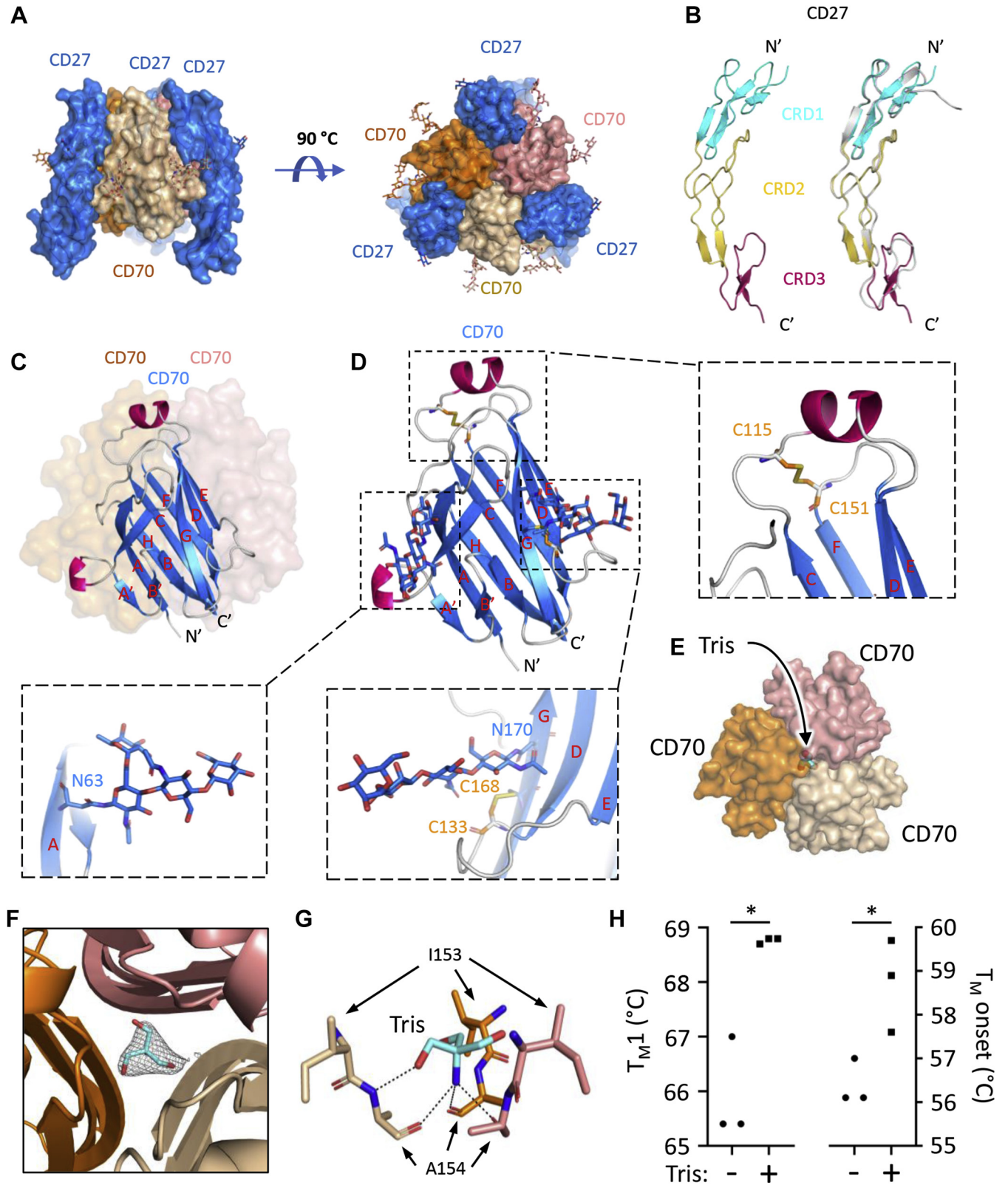

Figure 2. Overall structure of the human CD27:CD70 complex. *A*, the overall structure of human CD27:CD70 complex in the *side view* and *top view*. The glycosylation sites are shown as *sticks*. CD27 subunits are shown as *blue surface*. Homotrimeric CD70 in the center is shown as surface with each protomer colored differently (*light orange*, *dark orange*, and *salmon*). *B*, structure of CD27 from the CD27:CD70 complex is shown as *cartoon* with each CRD colored differently (CDR1, CRD2, and CRD3 in *cyan*, *yellow*, and *pink*, respectively). Alignment of the structures of CD27 from the CD27:CD70 complex (this report, in color) and the CD27:Fab complex (PDB entry 5TI5, in *gray*) shows moderate inter-CRD motion. *C*, structure of CD70 with two protomers shown as surface (*dark orange* and *salmon*) and one protomer shown as *cartoon* with each β-strand labeled (in *blue*). Key secondary elements in the loop regions are shown in *pink*. *D*, zoom in views of the carbohydrates (*blue sticks*) and disulfide bonds (*yellow sticks*) of CD70. Other structural elements were shown as in *C*. *E*–*G*, the

including salt bridges and hydrogen bonds involve residues contributed by CRD2 and CRD3 of CD27.

Epitope mapping of CD27 and CD70

To validate the atomic interactions observed in the structure of CD27:CD70 complex, we applied rational mutagenesis targeting key structural features of the complex and measured the binding of resulting muteins to their cognate protein partner by SPR. To do so, we designed and expressed 15 muteins of CD27 and 31 muteins of CD70. Most mutations tested were single substitutions, with the exception of two double substitutions developed to eliminate a disulfide bond by removing both cysteines forming the bond. Mutations had varying effects on the CD27:CD70 interaction.

Firstly, several engineered substitutions resulted in loss of expression. One N-linked glycosylation site in CD70 (N63, T65) was found to be essential for expression. In addition, removal of the CD70 surface-exposed disulfide between C133 and C168 greatly impaired CD70 expression, indicating that this structural disulfide is critical for the stability of the ligand (Fig. 4*A*). Mutagenesis of the N-glycosylation site N170Q decreases expression of CD70 and decreases binding to CD27 (Table 2). This site does not directly interact with CD27, but the inhibition of binding may result from solvent exposure of the C133-C168 disulfide bond and a subsequent increase in the lability of the bond, which stabilizes part of the CD27-binding interface (Fig. 4*A*). In CD70, substitutions of either P135 or D165 diminished expression and these two substitutions are proximal to the C133-C168 disulfide and enforce mainchain geometry around the bond (Fig. 4*A*). Disruption of the conserved TNF ligand family disulfide, C115-C151 in CD70, still led to protein expression, but this mutated variant did not bind CD27 (Table 2). Mutagenesis of the N-linked glycosylation site of CD27, branching from N95, did not significantly affect CD70 binding (Table 3). Consistent with studies using enzymatically deglycosylated CD27, the mutation N95A did not impair CD70 binding.

Our mutagenesis studies confirmed the importance of electrostatic interactions in the binding between CD27 and CD70. Charge-reversal substitutions for either E82 in CD27 or R83 in CD70 ablated measurable binding interaction, indicating the importance of this ionic interaction to the total binding energetics (Tables 2 and 3, Fig. 4*B*). In an even more conservative approach, alanine substitution at either position resulted in loss of binding, as did the R83K mutation of CD70 (Table 2). Position E82 in CD27 also simultaneously interacts with R138 from the neighboring CD70 monomer, which is coordinated by engagement of D74 residue of CD27 (Fig. 4*B*). This aspartate forms hydrogen bonds with residue S137 of CD70, further stabilizing the interaction (Fig. 4*B*). While S137A and S137K substitutions of CD70 have little effect on binding, the affinity of CD70-S137E binding to CD27 decreased by approximately fourfold due to an increase in the dissociation rate resulting from introduction of electrostatic repulsion with residue D74 of CD27 (Table 2 and Table S1). D74A mutant of CD27 showed weaker binding affinity to CD70 as indicated by heterogeneous kinetic binding curve (Table 3). R30 alanine substitution in CD27 resulted in approximately threefold weaker binding affinity by decreasing the complex association rate, possibly by destabilizing the conformation of H75 and D74 in CD27 (Fig. 4*B* and Table 3).

Positions S83 and S70 on CD27 are proximal to residue E82 on CD27 and form hydrogen bonds with residues Q61 and A80 of CD70, respectively (Fig. 4*C*). Alanine substitutions of either position 83 on CD27 or position 61 on CD70 both increased the dissociation rate and therefore weakened the affinity of the CD27-CD70 interaction by about twofold (Tables 2 and 3 and Table S1). Nearby, the hydroxyl group of residue S70 in CD27 forms a hydrogen bond with main chain oxygen of residue A80 in CD70 (Fig. 4*C*). The mutations A80L and A80V in CD70 showed altered and decreased binding to CD27 that cannot be quantitated by SPR, while A80R and A80F substitutions in CD70 showed ∼1.3 and ∼5-fold decreased binding affinity, respectively (Table 2). Our explanation for this behavior is that beta- or gamma-branched side chains at position 80 in CD70 will clash with CD27, but the elongated side chain of arginine can protrude from this close contact and does not deform the mainchain conformation and thus not impede the binding interaction.

The importance of another network of electrostatic interactions was also tested by mutagenesis. The acidic residue D114 of CD27 interacts with R144 of CD70, and both are stabilized by a network of hydrogen bonds from neighboring amino acids (Fig. 4*D*). Substitutions at either CD27 position 114 or CD70 position 144 disrupted binding kinetics, including conservative substitutions such as residue D114E of CD27 (Table 3). This suggests that the exact geometry of interaction is required at this site for measurable binding to occur. Mutagenesis of the surrounding CD27 residues N88, R113, T118, and D121 also disrupted binding (Table 3), as did mutagenesis of their interacting CD70 residues S178 and N180 (Fig. 4*D*, Table 2 and Table S1). CD70 mutant S146D disrupted binding but S146A did not, suggesting that longer side chains sterically impede binding. H148 substitutions increased the complex dissociation rate to varying degrees. Residue K115 in CD27 is proximal to this site, but the lysine side chain contact with CD70 is marginal, so alanine substitution at position 115 did not decrease the affinity (Fig. 4*D* and Table 3).

Both trimeric CD70 and sc-CD70-hIgG1 require further clustering to stimulate signaling

To gain greater understanding into the requirements of CD27 signaling, we used a T cell activation assay and observed that plate-bound trimeric wild-type CD70 induced IFNγ

Tris molecule sits in the center of CD70 homotrimer. *E*, Tris molecule bound (*cyan sticks*) within CD70 trimer with protomers shown as in *A*. *F*, polder omit map was contoured at 6.5 σ (*gray mesh*), of Tris molecule was shown as *cyan sticks*. *G*, Tris molecule (*cyan sticks*) makes polar contacts with I153 and A154 backbones from each CD70 protomer (*light orange*, *dark orange*, and *salmon sticks*). *H*, thermal stability measurements of the sc-CD70-WT-hIgG1 with PBS (−) and PBS containing 100 mM Tris (+). Unpaired *t* test indicates significant difference between two samples. $^{*}p < 0.05$.

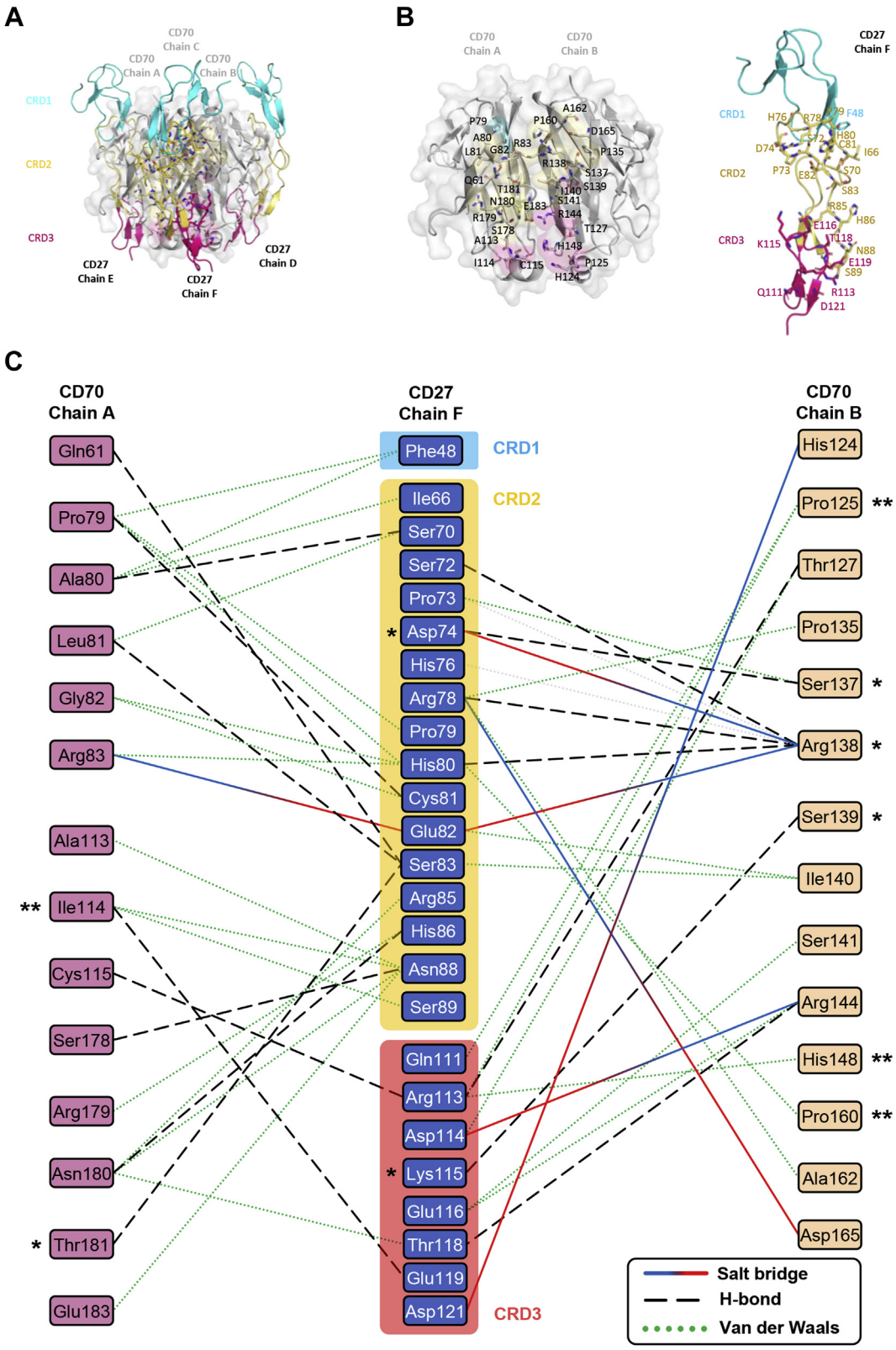

Figure 3. Binding interface between human CD27 and CD70. *A*, overall structure of the human CD27:CD70 complex. The homotrimeric CD70 in the center is colored as *gray surface*. CRD1, CRD2, and CRD3 of CD27 are shown as *cartoon* and colored as *cyan*, *yellow*, and *pink*, respectively. The residues directly involved in the CD27 (chain F) and CD70 (chains A and B) interaction interface are shown as *sticks*. *B*, open book view of the interface between CD70 and CD27 with interacting residue labeled. CD70, on *right*, is colored to match corresponding CD27 CRDs (*cyan*, CRD1; *yellow*, CRD2; *magenta*, CRD3). *C*, interaction diagram between two CD70 monomers and one CD27 molecule. Amino acids marked '*' are nonidentical but similar with mouse ortholog, and those marked '**' are divergent in mouse ortholog.

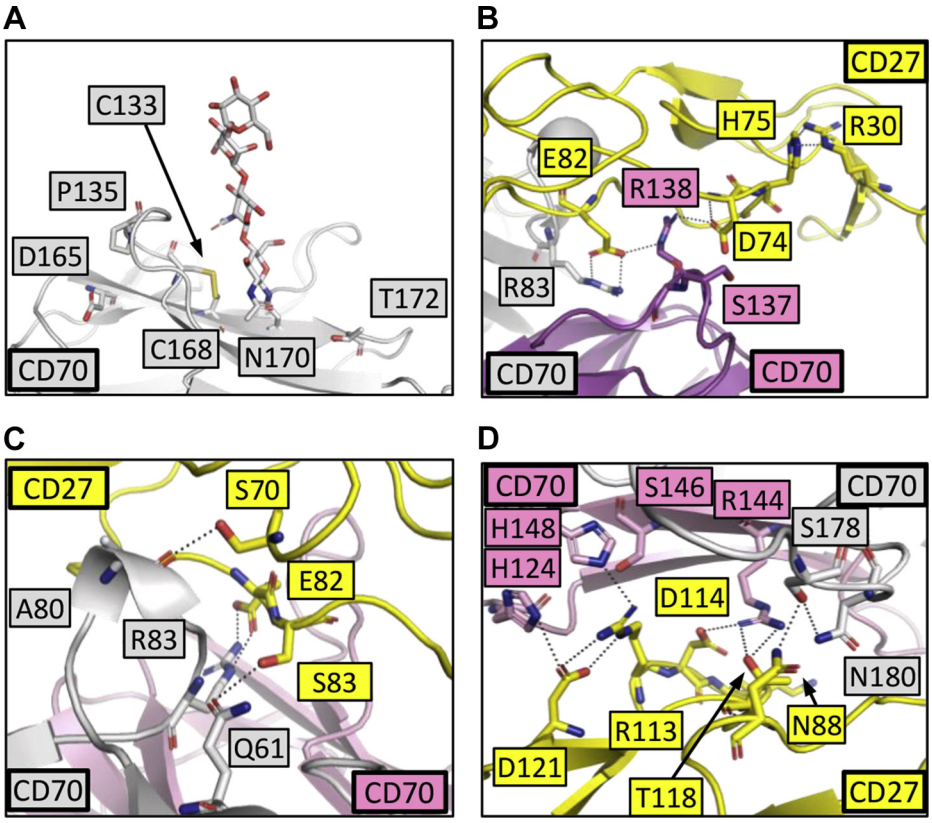

Figure 4. Structural analysis of the mutated residues within or close to the CD27:CD70 interface. Detailed views of important structure features observed in structure are shown from *A–D*. Two adjacent CD70 protomers are colored as *gray* and *light pink*. CD27 is colored as *yellow*. Key residues are shown as *sticks* and labeled. The glycans extended from residue N170 of CD70 are also shown as *sticks*. Polar contacts observed within the selected residues in the structure are shown as *black dashes*.

production in a concentration-dependent manner (Fig. 5*A*). The plate-bound trimeric CD70-induced IFNγ secretion was dependent on TCR stimulation as plate-bound CD70 had no effect in the absence of anti-CD3 antibodies. The dependence of CD70-induced activation on anti-CD3 antibody concentration and the lack of stimulation from treatment with anti-CD3 antibody alone demonstrate the synergistic relationship between TCR engagement and costimulation by CD70. Similar results were obtained in a *Jurkat* reporter assay measuring AP-1 transcriptional activity. AP-1 induction drives cytokine production by T cells, and as much as fourfold induction of the luciferase reporter was observed with plate-bound trimeric wild-type CD70 (Fig. 5*C*). However, no AP-1 activation was observed for cells treated with soluble trimeric CD70 (Fig. 5*C*).

These results suggest that trimeric CD70 sensitized T cell activation but required artificial clustering in a plate-bound form, leading us to utilize a sc-CD70-hIgG1 biologic, which has greater potential to cluster CD27. In the sc-CD70-hIgG1 construct used here, three concatenated CD70 sequences were fused to the N-terminus of hIgG1 Fc (Fig. 5*B* and Fig. S1*C*). The sc-CD70-hIgG1 construct largely improved the yield of purification from Expi293 cell cultures compared with the trimeric CD70 ligand (50 mg/l *versus* 5 mg/l). Sc-CD70-hIgG1 also significantly improved the homogeneity of the protein with most of the single chain CD70-hIgG1 existing as a symmetric peak in SEC (Fig. 5*B*).

We then compared the functional activity of plate-bound trimeric wild-type CD70 and sc-CD70-hIgG1 in a *Jurkat* reporter assay. Plate-bound sc-CD70-hIgG1 exhibited concentration-dependent induction of the luciferase reporter similar to plate-bound trimeric CD70 (Fig. 5*C*). However, soluble sc-CD70-hIgG1 clustering was still not strong enough to induce luciferase reporter in the *Jurkat* reporter assay (Fig. 5*C*).

Taken together, our data indicate that the trimeric or hexameric clustering by trimeric CD70 or sc-CD70-hIgG1 alone is not strong enough to trigger CD27-mediated signaling. CD70 requires higher-order assembly to stimulate CD27 activation (Fig. 5*D*). These results also align with the previous report showing that hexameric CD70 was not sufficient, and higher-order oligomerization of CD27 was necessary, for signaling activation (33).

Discussion

TNF ligands can be classified into three groups based on their sequences and structures (34). Group 1 TNF ligands are the conventional TNF ligands exhibiting the classical pyramidal homotrimeric structure. Group 1 TNF ligands include TNFα, LTα, LTβ, TRAIL, LIGHT, FasL, TL1A, RANKL, and CD40L, and crystal structures of human homologs of all these representative molecules have been determined (35–40).

Table 2
Binding kinetics of immobilized CD70 wild-type and mutants with wild-type CD27 (glycosylated) as analytes at the temperature of 37 °C

Sample	n	k_a (10^4 $M^{-1}s^{-1}$)	k_d (10^{-3} s^{-1})	K_D (nM)	Result
CD70 (WT)	6	3.66 (0.20)	4.41 (0.16)	121 (8)	Homogeneous kinetics
CD70-Q61A	6	3.30 (0.38)	6.76 (0.27)	205 (25)	
CD70-A80F	6	1.44 (0.33)	9.27 (0.44)	643 (151)	
CD70-A80R	6	1.66 (0.21)	2.70 (0.29)	163 (24)	
CD70-S137A	6	3.80 (0.54)	5.91 (0.10)	156 (22)	
CD70-S137E	6	2.83 (0.04)	14.90 (0.59)	526 (22)	
CD70-S137K	6	2.92 (0.18)	3.93 (0.16)	135 (10)	
CD70-S146A	6	3.59 (0.06)	4.17 (0.08)	116 (3)	
CD70-H148A	6	3.93 (0.07)	9.28 (0.29)	236 (9)	
CD70-H148E	4	5.37 (2.23)	20.40 (7.03)	380 (205)	
CD70-H148D	6	3.41 (0.30)	16.30 (1.81)	477 (68)	
CD70-A80L	2	–	–	–	Altered binding kinetics compared with CD70-WT[a]
CD70-N180A	2	–	–	–	
CD70-A80V	2	–	–	–	No binding[b]
CD70-R83A	2	–	–	–	
CD70-R83E	2	–	–	–	
CD70-R83K	2	–	–	–	
CD70-C115AC151A	2	–	–	–	
CD70-R144A	2	–	–	–	
CD70-R144E	2	–	–	–	
CD70-S146D	5	–	–	–	
CD70-N170Q	2	–	–	–	
CD70-S178A	2	–	–	–	
CD70-N180R	2	–	–	–	
CD70-N180W	2	–	–	–	
CD70-C133AC168A	2	–	–	–	Low expression[c]
CD70-N63Q	2	–	–	–	
CD70-T65A	2	–	–	–	
CD70-T172A	2	–	–	–	
CD70-D165R	3	–	–	–	
CD70-D165A	2	–	–	–	
CD70-P135A	2	–	–	–	

Avi-tagged Human CD70 wild-type and mutants were expressed in Expi293 cells and cell culture supernatants were captured onto anti-Avi surfaces. At least four independent expression batches were tested for CD70 mutants with homogeneous kinetic profiles. The number of replicate measurements is listed as n. Standard deviations are shown in parenthesis.
[a] Kinetics and affinity parameters were not reported due to weak binding.
[b] Expression was satisfactory (CD70 ligand capture of >15 RU), but no CD27 binding was observed.
[c] Expression levels were too low (CD70 ligand capture of <5 RU) to accurately assess CD27 binding.

Examples of group 2 TNF ligands include APRIL, BAFF, TWEAK, and EDA. Crystal structures of human APRIL, BAFF, and EDA were determined (41–43). Group 3 TNF ligands are the most structurally divergent members and include CD70, CD30L, GITRL, 4-1BBL, and OX40L (34). Cocrystal structures of human GITRL, 4-1BBL, and OX40L with their respective receptors were published previously, but this report is the first publication of the cocrystal structure of CD70 (34, 44–47). The overall trimeric CD70 assembly adopts a "blooming flower" structural arrangement that most resembles OX40L (Fig. S3*C*). The CD70 C115-C151 disulfide bond resembles the disulfide bonds of TNFα, LIGHT, FasL, and TL1A, which connect the CD and EF loops. (Fig. S3). The CD70 C133-C168 disulfide bond connects the G strand and DE loop. The position of this disulfide bond is unique among known TNF ligand structures to date. A separate disulfide

Table 3
Binding kinetics of CD27 wild-type (glycosylated) and mutants with immobilized CD70 at the temperature of 37 °C

Analyte	n	k_a (10^4 $M^{-1}s^{-1}$)	k_d (10^{-3} s^{-1})	K_D (nM)	Result
CD27 (WT)	3	3.31 (0.42)	4.47 (0.43)	135 (22)	Homogeneous kinetics
CD27-R30A	3	1.34 (0.07)	4.70 (0.34)	351 (31)	
CD27-S83A	3	3.36 (0.36)	8.54 (0.55)	254 (32)	
CD27-N95A	3	7.25 (0.17)	7.26 (0.04)	100 (2)	
CD27-K115A	3	3.45 (0.32)	3.51 (0.04)	102 (9)	
CD27-S70A	1	–	–	–	Altered kinetics compared with CD27-WT[a]
CD27-D74A	1	–	–	–	
CD27-N88A	1	–	–	–	
CD27-R113A	1	–	–	–	
CD27-D114E	1	–	–	–	
CD27-D114R	1	–	–	–	
CD27-T118E	1	–	–	–	
CD27-T118R	3	–	–	–	
CD27-D121A	1	–	–	–	
CD27-E82R	1	–	–	–	No binding
CD27-E82A	1	–	–	–	

[a] Kinetics and affinity parameters were not reported due to weak binding (R113A, D114R, T118E, T118R), heterogeneous kinetics (D74A, N88A, D114E, D121A), or slow association (S70A). Triple independent experiments were performed to measure the binding affinities of mutants with homogeneous kinetic profiles. Standard deviations are shown in parenthesis. The number of replicate measurements is listed as n.

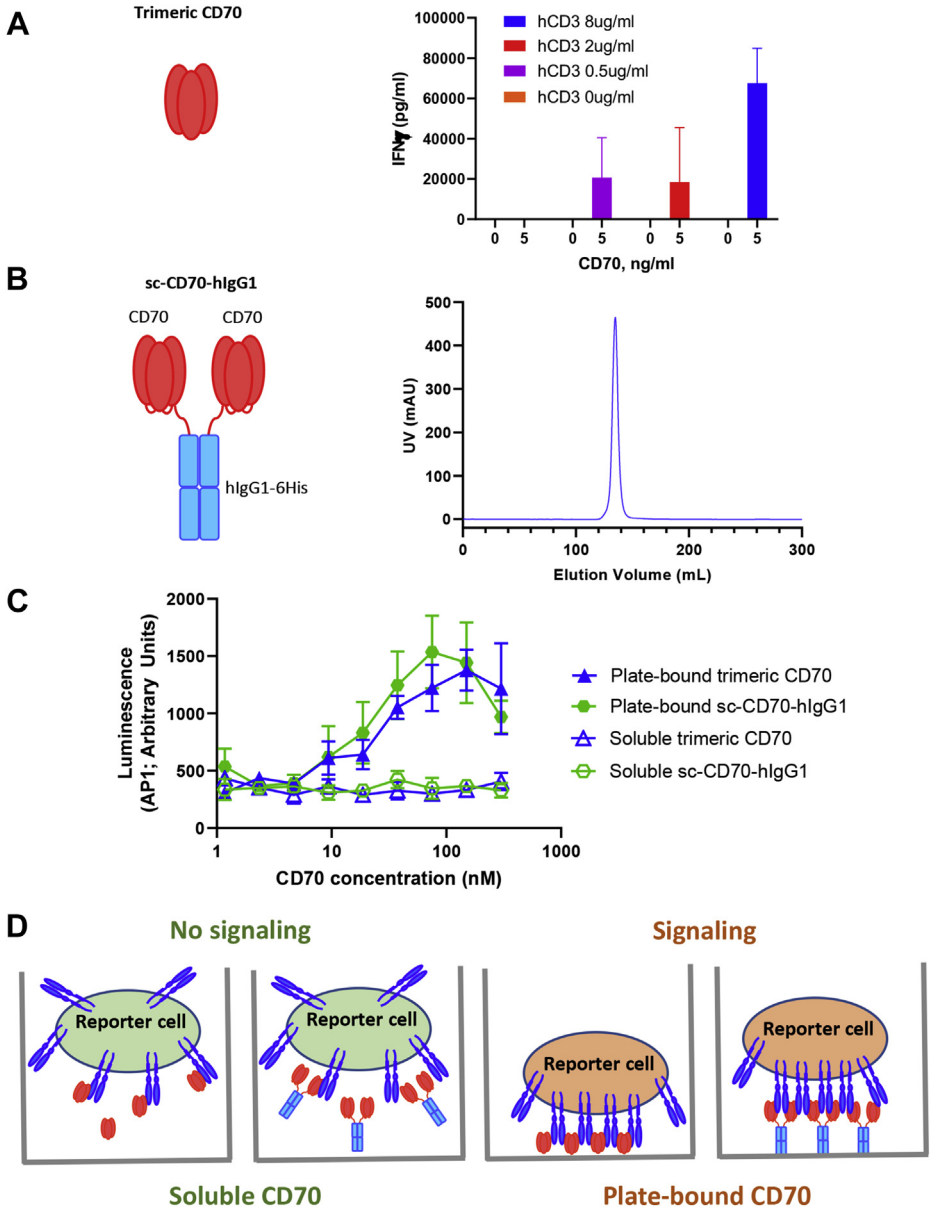

Figure 5. Both trimeric and sc-CD70-hIgG1 require plate binding to stimulate signaling. *A*, overall architecture of trimeric wild-type CD70 and its effect in stimulating primary T cells in the presence of different concentrations of anti-CD3 stimulation. *B*, overall architecture and SEC purification profile of the wild-type sc-CD70-hIgG1 fusion protein. *C*, *Jurkat* cell signaling assay for the plate-bound or soluble wild-type trimeric CD70 and sc-CD70-hIgG1 showed that the soluble CD70 was not strong enough to induce signaling, whereas the plate-bound CD70 induce significant signaling in the reporter cells. *D*, *cartoon* diagram showed that *Jurkat* cell expressing CD27 was activated by plate-bound CD70. Plate-bound CD70 but not the soluble CD70 is able to form higher-order clustering to more efficiently induce *Jurkat* reporter cell signaling.

bond is present in the structure of human OX40L, which connects the B and H strands (Fig. S3*B*). These unique disulfide bonds reflect the structural divergence of group 3 TNF ligands.

The overall structure of CD27:CD70 complex adopts a classical 3:3 interaction mode. Since CD27 can form a homodimer *in vivo* through a disulfide bridge mediated by the C185 in the stalk region (8, 28), CD27 and CD70 may participate in more complex assemblies to modulate signaling (Fig. 6). Notably, some other TNF receptors, for example, mouse HVEM, also have an unpaired cysteine in the stalk region. We observed that at low concentrations neither soluble trimeric nor hexameric CD70 triggered measurable IFNγ secretion, whereas plate-bound CD70 did stimulate secretion from primary human T-cells *in vitro*. The prior report of *in vitro* T-cell activation by treatment with solution-phase trimeric CD70 or hexameric CD70-Fc fusion protein (4) required much higher concentration than those used here, suggesting that receptor clustering can occur with sufficient saturation ligand engagement in a dose-dependent manner (23). These findings for CD27 activation are consistent with existing models of TNFR signaling where formation of a macromolecular assembly containing higher-order receptor clustering is necessary for signaling (33).

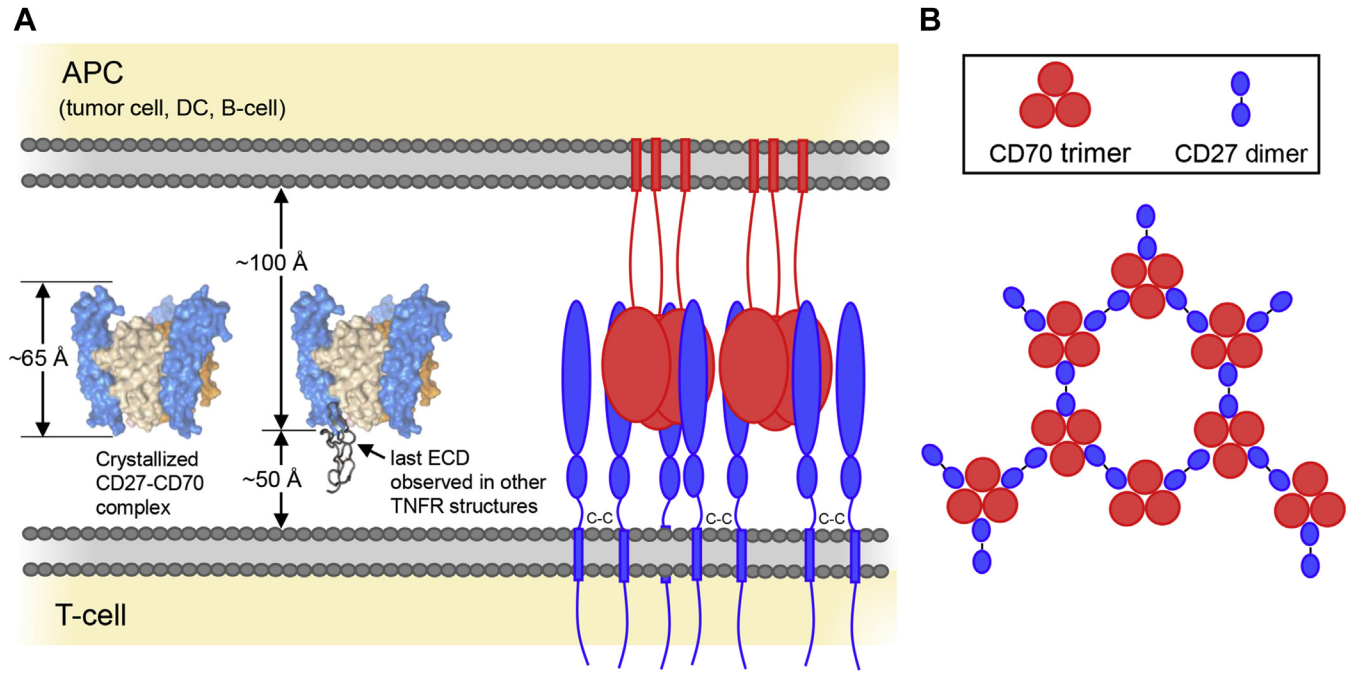

Figure 6. Conceptual diagram of CD27-CD70 complex within immunological synapse. *A*, comparison of crystallized complex with theoretical diagram of ECD. Complex dimension estimates are shown and compared with intermembrane distance for immunological synapse. In *gray cartoon*, the C-terminal CRD observed in other TNFR structures is depicted at the C-terminus of the crystallized CD27 construct in complex with CD70 (4-1BB, chain A from PDB ID 5WJF shown here). On *right*, *cartoon* diagram of complex depicting complete sequences for CD27 and CD70. Dimeric CD27 shown with membrane-proximal intermolecular disulfide involving Cys185. Transmembrane helices shown as *colored rectangles* passing across cell membrane lipid bilayer. *B*, multivalent complex diagram as viewed in plane with cell membranes. Through engagement of dimeric CD27 by trimeric CD70, larger arrays may form that will enhance receptor clustering to stimulate signaling.

Comparison of CD27:CD70 signaling complex structure with prior crystal structures of CD27 allows interrogation of previously proposed mechanistic models of antagonist molecules. Two crystal structures have been reported with CD27 bound to Fab fragments of inhibitory antibodies (29, 48). One antibody, 2191, competes for CD70 binding with the interaction epitope that overlaps with the CD70-binding site on CD27 in our structure (Fig. S4*A*). The other antibody, 2177, inhibits CD27 signaling but does not block soluble CD70 binding *in vitro*. The crystal structure of this Fab bound to CD27 reveals a binding site on CRD1 that does not clash with the CD70-binding interface identified here. It was proposed previously that 2177 IgG antibody binds to CD27 and inhibits the interaction of cell-bound CD70 by excluding CD27 from close contact with the CD70-expressing cell (Fig. S4*B*). This model indicates that sufficient proximity between the plasma membranes of the two opposing cells is a crucial factor for CD27:CD70 engagement. To evaluate the CD27:CD70 assembly within the cellular context, we constructed a model of the entire extracellular domains of the CD27:CD70 complex (Fig. 6*A*). To model the region between the N-terminal transmembrane helix of CD70 and the first-ordered residue present in the crystal structure (G54), we built an extended 14-residue linker. In the absence of secondary structure data for this region, we built a polypeptide chain as a fully extended structure to provide a maximum possible dimension from point anchored at the cell membrane. Such extended linker would span roughly 40 Å. In the case of CD27, the linker (67 residues) between the C-terminus of CRD3 and the transmembrane helix lacks sequence homology to any published structure. We propose that the sequence between CRD3 and the transmembrane helix of CD27 adopts some compact structure consistent with the TNF receptor superfamily at large (Fig. 6*A*), and hence the structure of 4-1BB was used to model the complete ectodomain of CD27. With CD70 homotrimers engaging CD27 homodimers, these binding partners may form large arrays, which could increase the density of clustered receptors and amplify the costimulatory signal (Fig. 6*B*).

Our model can be at least partially explained with the reports on CD70-binding antagonists. The epitope of one of such antagonistic antibodies, ARGX-110, has been mapped to the CD70 peptide H107-S117 (49, 50). Six residues of this peptide are obscured within the CD70 homotrimer, but the exposed residue I114 contacts loop N88-G90 of CD27. Occupancy of this site by ARGX-110 would therefore produce a steric clash with CD27 (Fig. S4*C*).

Several naturally occurring sequence variants of CD27 and CD70 have been reported exhibiting a range of associated phenotypes. We have investigated these variants to identify the structural bases of their observed effects on CD27-CD70 signaling. Some reported disease-correlated sequence variants in CD27 disrupt disulfide bonds in the molecule. The C53Y substitution correlates with pathology in LPFS2 (lymphoproliferative syndrome 2) (51). This substitution removes one structural disulfide within CRD1 of CD27. An analogous mutation, C96Y, removes a structural disulfide bond in CRD2 (13). The loss of a structural disulfide bond would likely result

in a significant loss of protein stability, which is consistent with the apparent decrease in CD27 expression and a loss-of-function phenotype *in vivo* (13).

Another substitution in CD27, R78W, was reported in one patient with severe EBV infection (13). This arginine forms electrostatic and hydrogen-bond interaction with CD70 (Fig. 3*C*), so a substitution for a bulky aromatic tryptophan side chain at this site would disrupt these favorable ligand:receptor associations. A more subtle substitution identified in CRD1 of CD27 is A59T (52). This variant is not known to correlate with any physiological outcome and based on our structure this position does not interact with CD70. From a structural perspective, either alanine or threonine encoded at this position would be well tolerated and would not impair CD27:CD70 signaling. A final reported clinically relevant substitution R107C decreases CD27 expression (13). This substitution will not impair CD70 binding but would introduce a surface-exposed unpaired cysteine, which is unstable due to the reactivity of the free thiol group.

In CD70, one sequence conflict, A154V, has been reported in Uniprot (53). In the crystal structure reported here, position 154 is buried at the trimeric axis of CD70. In the construct used for these structural studies, an alanine is encoded at this position. The proximity of this position with the other CD70 chains would result in a clash if valine was present here. No phenotypic effect of this substitution has been reported to date. Another observed sequence variance is a deletion of the C-terminal amino acids from either position 179 or 186 onward (11), which eliminates the central H β-strands at the CD70 trimer core. The importance of this strand to the CD70 structure explains why this deletion results in loss of expression and the subsequent reported clinical outcomes (11). A recent case study identified disease-correlated substitutions T111M and S146I in CD70 (54). Both are reported to decrease expression of CD70. From the crystal structure we observe that the larger side chains substituted at these positions will result in steric clashes with CD27 or with loops on CD70 that engage with CD27. This suggests that the clinical consequences of these substitutions are not only a result of expression levels but also result from a decrease in binding affinity.

In conclusion, this report identifies the key residue-level interactions between CD27 and CD70. The structure also enables the rational design of novel protein biologics and small molecules to modulate the CD27:CD70 axis for potential therapeutic applications.

Experimental procedures

Protein expression and purification

Gene fragments encoding the human CD27 ORF residues A23–S127 (Uniprot ID P26842) with a C-terminal fused peptide bearing amino acid sequence of "GSGHHHHHH" and human CD70 ORF residues Q45–P193 (Uniprot ID P32970) with a N-terminal fused peptide bearing amino acid sequence of "HHHHHHGSG" were cloned into a mammalian expression vector (pTT5). The expression vectors were transfected into Expi293 cell for protein expression. For human CD27 protein expression, kifunensine (Sigma-Aldrich) at a final concentration of 5 μM was supplemented to the Expi293 cell (Thermo Fisher) culture during transfection and culturing to inhibit the α-mannosidase I-mediated glycosylation as previously described (55). Single-chain CD70 was fused with human IgG1 Fc followed by a 6× His tag. All constructs were transfected into Expi293 cells with 1 mg plasmid DNA per liter of cell culture. The transfected cell cultures were harvested 5 days after transfection and subjected to Ni sepharose His-Trap Excel column (Cytiva) purification. For human CD27 protein purification, the protein eluate after Ni sepharose purification was concentrated to 2 ml and subjected to Endoglycosidase H (Endo H; New England Biolabs) digestion overnight at 4 °C. Human CD27 protein after Endo H digestion and human CD70 after Ni sepharose purification were filtered and injected onto a Superdex 200 pg preparative SEC column (Cytiva) equilibrated with the buffer containing 20 mM HEPES pH 7.4, 150 mM NaCl.

Analytical size exclusion chromatography

aSEC was performed using an Agilent HPLC 1100 with a Superdex 200 Increase 5/150 GL column (Cytiva). The system was equilibrated with Tris-buffered saline at pH 7.5 and samples were injected and run at 0.15 ml/min. Absorbance was measured at 280 nm. Molecular weight standards (Biorad) were run separately using identical settings.

Capillary electrophoresis

Analysis of all samples was performed on the LabChip GXII touch HT (PerkinElmer) according to the manufacturer's protocol. Briefly, denatured protein was prepared by mixing 2 μl protein sample (1 mg/ml) with 14 μl of the denaturation solution (Protein Express Sample Buffer) provided by the manufacturer in the presence of 23 mM iodoacetamide (Sigma) for nonreducing condition or 34 mM DTT (Thermo Scientific) for reducing condition. The mixture was heated at 75 °C for 5 min and the samples run under both reducing and nonreducing conditions. The denatured protein was electrokinetically loaded directly into the chip from a microtiter plate (Bio-Rad Laboratories). The experiment was run using LabChip GX touch software (PerkinElmer) and data were analyzed using LabChip GX Reviewer (PerkinElmer).

Differential scanning calorimetry

DSC measurements were performed using a MicroCal VP Cap DCS instrument (Malvern Pananalytical). Sample measurements in the DSC were made at a concentration of 1.0 mg/ml protein. The thermograms were generated by scanning the temperature from 10 to 110 °C at a rate of 60 °C per hour. Peak fitting of the thermograms, calculation of unfolding transition point (Tm values) and Transition Onset (T-onset) were performed using Origin 7 (Originlab) software. Tm_1 is the lowest observed thermal transition. For each condition, three datapoints from two experiments were combined and analyzed together. *p*-Values were calculated using unpaired two-tailed *t* test (Graphpad Prism 9.0.0).

ASBMB

SPR analysis of CD27 binding to CD70

The affinities between CD27 and CD70-His-Avi were determined on a Biacore 8K SPR instrument (Cytiva Life Sciences) loaded with a Series S CM4 sensor chip (Part # 29104989) with amine-coupled polyclonal rabbit anti-Avi-Tag antibody (Genscript Corp, CAT# A0067440) on the surface of the chip. This includes interactions between glycosylated and deglycosylated wild-type CD27 against wild type CD70-His-Avi, glycosylated CD27 mutants against wild-type CD70-His-Avi, and glycosylated wild-type CD27 against CD70-His-Avi mutants. This also includes analyses using supernatant and/or purified proteins. For supernatant samples, if ligand capture achieved less than 15 RU, these were considered poorly expressing samples and were excluded from further analysis.

The sensor chip surface was prepared with 1xHBSP+ (0.01 M HEPES pH 7.4, 0.15 M NaCl, 0.05% v/v Surfactant P20) running buffer. All channels and flow cells were activated with a 1:1 (v/v) mix of 0.4 M 1-ethyl-3-(3-dimethylaminopropyl) carbodiimide hydrochloride (EDC) and 0.1 M N-hydroxysuccinimide (NHS) for 7 min at 10 μl/min. Anti-Avi-Tag antibody was then amine-coupled at 30 μg/ml in 10 mM Acetate pH 4.5 for 7 min at 20 μl/min, and the surface was blocked with 0.1 M ethylenediamine (EDA) in 0.2 M borate buffer pH 8.5 for 7 min at 10 μl/min. The surface was then regenerated with 75 mM phosphoric acid for 30 s, three times, at 10 μl/min. The resulting immobilization levels were 38,766 ± 233 RU across the 16 flow cells.

Multicycle kinetic assays were performed at 37 °C with 1xHBSP+ supplemented with 1 g/l bovine serum albumin (BSA) as running buffer. Purified CD70-His-Avi were captured at 0.3 μg/ml for CD27 mutant screening and CD70 mutant screening, and at 0.2 μg/ml for n = 3 kinetics with glycosylated and deglycosylated CD27. CD70-His-Avi supernatants were diluted 5× in running buffer for capture. CD70 proteins were captured for 1 min at 10 μl/min on flow-cell 2 of each channel. Buffer was injected over flow cell 1 of each channel for reference subtraction. CD27 was then injected at concentrations of 0, 8.0, 40, 200, 1000, and 5000 nM. Dissociation was monitored for 5 min. At the end of every cycle, the surface was regenerated with 75 mM phosphoric acid for 30 s, three times, at 10 μl/min.

Since the CD27 analyte is monomeric, sensorgram data were double-referenced and fit to a *1:1 Langmuir with mass transport* kinetics model in Biacore 8K evaluation software [Biacore 8K Evaluation Software Version 1.1.1.7442] to yield kinetic rate constants. Kinetics for glycosylated and deglycosylated wildtype CD27 against CD70, as well as for relevant CD70 mutants and CD27 mutants, were performed in at least n = 3 (replicates of independent analyte dilution series). Analyses were performed by a combination of Biacore 8K internal software and BiaEvaluation Software 4.0.

Crystallization

To crystallize CD27 in complex with CD70, we prepared a batch of protein with a CD27:CD70 monomer molar ratio of 1:1, calculated using measured A_{280} and the predicted molar extinction coefficient for each construct. The mixture of CD27 and CD70 proteins was then concentrated to 10 mg/ml in HEPES-buffered saline at pH 7.5. This mixture was then mixed with EndoH (NEB) at a final concentration of 0.3 units/μl. Hanging drops were then prepared using a NT8 liquid-handling system (FORMULATRIX) combining 100 nl protein solution with 100 nl well solution. Crystals were obtained from drops at 18 °C with well solution consisting of 100 mM tris hydrochloride pH 8 with 40% 2-methyl-2,4-pentanediol. Crystals were frozen without addition of cryoprotectant due to the high concentration of 2-methyl-2,4-pentanediol present in the crystallization drop.

Data collection

Crystals were snap-frozen by plunging in liquid nitrogen and shipped to Canadian Light Source for data collection at the Canadian Macromolecular Crystallography Facility, beamline 08ID-1. Data collection was performed by staff from IMCA-CAT, beamline 17-ID-B. Frames were collected with 0.25° oscillation, 720 total frames from one crystal in dataset. Data were processed and anisotropically truncated using AutoPROC version 1.1.7 (56).

Molecular replacement and structural determination

Data were phased by molecular replacement using initial models identified using the SwissModel server (57). An initial molecular replacement solution was found for the CD70 trimer model derived from PDB entry 2RE9 (30), and subsequently three copies of CD27 monomer derived from PDB entry 5Tl5 were placed (29). This phased model was further refined using both PHENIX (58) and BUSTER (56). Manual model building was performed using COOT (59).

Structure analysis

The completed model was analyzed using measurement and get_area functions in PyMOL version 2.3.0 (https://pymol.org/2/support.html?). For TNF ligand trimer angle and dihedral analysis, measurements were taken between the N- and C-terminal Cα of β-strand 1 from each TNF ligand monomer. For hTNFα, PDB ID 3ALQ, these residues are V13 and A18. For hGITRL, these residues are M59 and F62. For hOX40L, these residues are S61 and K70. For hCD70, these residues are V57 and T65.

Plate-bound anti-CD3 T cell interferon-γ release assay

The costimulatory capability of CD70 protein on primary human T cells activation upon T cell receptor engagement was evaluated using plate-bound anti-CD3 antibody (Ultra-LEAF(TM) purified anti-human CD3 [OKT3], Biolegend, # 317326) as the TCR ligand. Anti-CD3 antibody and various concentration of CD70 protein in sterile PBS were added into MaxiSorp Immuno plates (Thermo Scientific, #439454) and incubated at 4 °C overnight. Next day the plates were washed three times with fresh PBS. Human Peripheral Blood pan-T cells (StemCell, # 70024) were added into the precoated

plates and incubated at 37 °C, 5% CO_2 for 3 days. The activation of T cells was evaluated by measuring the IFNγ production with V-PLEX Human IFN-γ Kit (Meso Scale Diagnostics, #K151QOD-4) following the manufacturer's protocol. The data represent three independent biological replicates (mean± standard error).

Jurkat cell luciferase signaling assay

Nunc MaxiSorp 96-well plates (Thermo Fisher # 44-2404-21) were coated overnight at 4°C with 1 μg/ml anti-human CD3 antibody (BD catalog # 555336) and dilutions of CD70 protein within 50 μl of PBS. The following day, plates were washed with PBS, and 50,000 *Jurkat* reporter cells were added in RPMI 1640 (Thermo Fisher # 72400047) with 10% FBS. The *Jurkat* reporter was stably transfected with an AP-1-dependent luciferase reporter. After a 4-h incubation at 37°C, One-Glo luciferase reagent (Promega # E6120) was added to the cells, incubated with gentle shaking for 5 min, and luminescence was measured by a Tecan Spark plate reader.

Data availability

The structures presented in this paper have been deposited in the Protein Data Bank (PDB) with the ID code 7KX0.

Supporting information—This article contains supporting information.

Acknowledgments—We want to thank Dr Steven C. Almo for stimulating and valuable advice to revise the manuscript. We also want to thank Dr Dirk M. Zajonc and Dr Aruna Bitra for valuable suggestions on the manuscript.
Part or all of the research described in this paper was performed using beamline 08ID-1 at the Canadian Light Source, a national research facility of the University of Saskatchewan, which is supported by the Canada Foundation for Innovation (CFI), the Natural Sciences and Engineering Research Council (NSERC), the National Research Council, the Canadian Institutes of Health Research, the Government of Saskatchewan, and the University of Saskatchewan. Use of the IMCA-CAT beamline 17-ID (or 17-BM) at the Advanced Photon Source was supported by the companies of the Industrial Macromolecular Crystallography Association through a contract with Hauptman-Woodward Medical Research Institute.
This research used resources of the Advanced Photon Source, a U.S. Department of Energy (DOE) Office of Science User Facility operated for the DOE Office of Science by Argonne National Laboratory under Contract No. DE-AC02-06CH11357.
This study makes use of data generated by the Blueprint Consortium. A full list of the investigators who contributed to the generation of the data is available from www.blueprint-epigenome.eu. Funding for the project was provided by the European Union's Seventh Framework Program (FP7/2007-2013) under grant agreement no 282510 – BLUEPRINT.
The research was funded by Pfizer Inc.

Author contributions—W. L., Z. M., L. M., and J. C.-R. conceptualization; W. L. and Z. M. data curation; W. L. and Z. M. formal analysis; L. M. and J. C.-R. funding acquisition; W. L., Z. M., C. W., K. C. L., M. L., V. R., I. L. A., A. N., E. P., P. K. D., D. O., H. W., R. C. R., and C. M. A. investigation; L. M. and J. C.-R. methodology; W. L., Z. M., L. M., and J. C.-R. project administration; L. M. and J. C.-R. resources; L. M. and J. C.-R. supervision; W. L., Z. M., C. W., K. C. L., M. L., V. R., I. L. A., A. N., E. P., P. K. D., D. O., H. W., R. C. R., C. M. A., L. M., and J. C.-R. validation; W. L. and Z. M. visualization; W. L., Z. M., L. M., and J. C.-R. writing—original draft; W. L., Z. M., K. C. L., M. L., A. N., P. K. D., H. W., L. M., and J. C.-R. writing—review and editing.

Conflict of interest—The authors declare no conflict of interest on the published contents in this paper.

Abbreviations—The abbreviations used are: aSEC, analytical size-exclusion chromatography; BSA, albumin; CGE, capillary gel electrophoresis; CRD, cysteine-rich domain; cSMAC, central supramolecular activation clusters; EBV, Epstein–Barr virus; EC_{50}, half maximal effective concentration; EDA, ethylenediamine; Fc, fragment crystallizable; k_a, association rate constant; k_d, dissociation rate constant; K_D, equilibrium dissociation constant; LPFS2, lymphoproliferative syndrome 2; NHS, N-hydroxysuccinimide; pSMAC, peripheral supramolecular activation clusters; sc-CD70-hIgG1, single-chain CD70-human IgG1; SEC, size-exclusion chromatography; SPR, surface plasmon resonance; TNF, tumor necrosis factor; TRAF, TNF receptor associated factor; WT, wild type.

References

1. Han, B. K., Olsen, N. J., and Bottaro, A. (2016) The CD27-CD70 pathway and pathogenesis of autoimmune disease. *Semin. Arthritis Rheum.* **45**, 496–501
2. Hintzen, R., De Jong, R., Lens, S., Brouwer, M., Baars, P., and Van Lier, R. (1993) Regulation of CD27 expression on subsets of mature T-lymphocytes. *J. Immunol.* **151**, 2426–2435
3. Buchan, S. L., Rogel, A., and Al-Shamkhani, A. (2018) The immunobiology of CD27 and OX40 and their potential as targets for cancer immunotherapy. *Blood* **131**, 39–48
4. Thiemann, M., Richards, D. M., Heinonen, K., Kluge, M., Marschall, V., Merz, C., Redondo Müller, M., Schnyder, T., Sefrin, J. P., Sykora, J., Fricke, H., Gieffers, C., and Hill, O. (2018) A single-chain-based hexavalent Cd27 agonist enhances T cell activation and induces anti-tumor immunity. *Front. Oncol.* **8**, 387
5. Kato, K., Chu, P., Takahashi, S., Hamada, H., and Kipps, T. J. (2007) Metalloprotease inhibitors block release of soluble CD27 and enhance the immune stimulatory activity of chronic lymphocytic leukemia cells. *Exp. Hematol.* **35**, 434–442
6. Zhou, Y., Liu, X., Xu, L., Tseng, H., Cao, Y., Jiang, J., Ciccarelli, B. T., Yang, G., Patterson, C. J., Hunter, Z. R., and Treon, S. P. (2011) Matrix metalloproteinase-8 is overexpressed in Waldenstrom's macroglobulinemia cells, and specific inhibition of this metalloproteinase blocks release of soluble CD27. *Clin. Lymphoma Myeloma Leuk.* **11**, 172–175
7. Denoeud, J., and Moser, M. (2011) Role of CD27/CD70 pathway of activation in immunity and tolerance. *J. Leukoc. Biol.* **89**, 195–203
8. Yamamoto, H., Kishimoto, T., and Minamoto, S. (1998) NF-κB activation in CD27 signaling: Involvement of TNF receptor-associated factors in its signaling and identification of functional region of CD27. *J. Immunol.* **161**, 4753–4759
9. Akiba, H., Nakano, H., Nishinaka, S., Shindo, M., Kobata, T., Atsuta, M., Morimoto, C., Ware, C. F., Malinin, N. L., and Wallach, D. (1998) CD27, a member of the tumor necrosis factor receptor superfamily, activates NF-κB and stress-activated protein kinase/c-Jun N-terminal kinase via TRAF2, TRAF5, and NF-κB-inducing kinase. *J. Biol. Chem.* **273**, 13353–13358
10. Hauer, J., Püschner, S., Ramakrishnan, P., Simon, U., Bongers, M., Federle, C., and Engelmann, H. (2005) TNF receptor (TNFR)-associated factor (TRAF) 3 serves as an inhibitor of TRAF2/5-mediated activation of

the noncanonical NF-κB pathway by TRAF-binding TNFRs. *Proc. Natl. Acad. Sci. U. S. A.* **102**, 2874–2879
11. Izawa, K., Martin, E., Soudais, C., Bruneau, J., Boutboul, D., Rodriguez, R., Lenoir, C., Hislop, A. D., Besson, C., Touzot, F., Picard, C., Callebaut, I., de Villartay, J. P., Moshous, D., Fischer, A., *et al.* (2017) Inherited CD70 deficiency in humans reveals a critical role for the CD70–CD27 pathway in immunity to Epstein-Barr virus infection. *J. Exp. Med.* **214**, 73–89
12. Abolhassani, H., Edwards, E. S., Ikinciogullari, A., Jing, H., Borte, S., Buggert, M., Du, L., Matsuda-Lennikov, M., Romano, R., and Caridha, R. (2017) Combined immunodeficiency and Epstein-Barr virus–induced B cell malignancy in humans with inherited CD70 deficiency. *J. Exp. Med.* **214**, 91–106
13. Alkhairy, O. K., Perez-Becker, R., Driessen, G. J., Abolhassani, H., Van Montfrans, J., Borte, S., Choo, S., Wang, N., Tesselaar, K., Fang, M., Bienemann, K., Boztug, K., Daneva, A., Mechinaud, F., Wiesel, T., *et al.* (2015) Novel mutations in TNFRSF7/CD27: Clinical, immunologic, and genetic characterization of human CD27 deficiency. *J. Allergy Clin. Immunol.* **136**, 703–712.e710
14. Jacobs, J., Zwaenepoel, K., Rolfo, C., Van den Bossche, J., Deben, C., Silence, K., Hermans, C., Smits, E., Van Schil, P., Lardon, F., Deschoolmeester, V., and Pauwels, P. (2015) Unlocking the potential of CD70 as a novel immunotherapeutic target for non-small cell lung cancer. *Oncotarget* **6**, 13462–13475
15. Aftimos, P., Rolfo, C., Rottey, S., Offner, F., Bron, D., Maerevoet, M., Soria, J.-C., Moshir, M., Dreier, T., and Van Rompaey, L. (2017) Phase I dose-escalation study of the anti-CD70 antibody ARGX-110 in advanced malignancies. *Clin. Cancer Res.* **23**, 6411–6420
16. Wajant, H. (2016) Therapeutic targeting of CD70 and CD27. *Expert Opin. Ther. Targets* **20**, 959–973
17. Lens, S. M., Drillenburg, P., Den Drijver, B. F., Van Schijndel, G., Pals, S. T., Van Lier, R. A., and Van Oers, M. H. (1999) Aberrant expression and reverse signalling of CD70 on malignant B cells. *Br. J. Haematol.* **106**, 491–503
18. Riether, C., Schürch, C. M., Bührer, E. D., Hinterbrandner, M., Huguenin, A.-L., Hoepner, S., Zlobec, I., Pabst, T., Radpour, R., and Ochsenbein, A. F. (2017) CD70/CD27 signaling promotes blast stemness and is a viable therapeutic target in acute myeloid leukemia. *J. Exp. Med.* **214**, 359–380
19. van Gisbergen, K. P., van Olffen, R. W., van Beek, J., van der Sluijs, K. F., Arens, R., Nolte, M. A., and van Lier, R. A. (2009) Protective CD8 T cell memory is impaired during chronic CD70-driven costimulation. *J. Immunol.* **182**, 5352–5362
20. Tesselaar, K., Arens, R., van Schijndel, G. M., Baars, P. A., van Der Valk, M. A., Borst, J., van Oers, M. H., and van Lier, R. A. (2003) Lethal T cell immunodeficiency induced by chronic costimulation via CD27-CD70 interactions. *Nat. Immunol.* **4**, 49–54
21. Arens, R., Schepers, K., Nolte, M. A., Van Oosterwijk, M. F., Van Lier, R. A., Schumacher, T. N., and Van Oers, M. H. (2004) Tumor rejection induced by CD70-mediated quantitative and qualitative effects on effector CD8+ T cell formation. *J. Exp. Med.* **199**, 1595–1605
22. Keller, A. M., Schildknecht, A., Xiao, Y., van den Broek, M., and Borst, J. (2008) Expression of costimulatory ligand CD70 on steady-state dendritic cells breaks CD8+ T cell tolerance and permits effective immunity. *Immunity* **29**, 934–946
23. Rowley, T. F., and Al-Shamkhani, A. (2004) Stimulation by soluble CD70 promotes strong primary and secondary CD8+ cytotoxic T cell responses *in vivo*. *J. Immunol.* **172**, 6039–6046
24. Buchan, S. L., Fallatah, M., Thirdborough, S. M., Taraban, V. Y., Rogel, A., Thomas, L. J., Penfold, C. A., He, L.-Z., Curran, M. A., and Keler, T. (2018) PD-1 blockade and CD27 stimulation activate distinct transcriptional programs that synergize for CD8+ T-cell–driven antitumor immunity. *Clin. Cancer Res.* **24**, 2383–2394
25. Burris, H. A., Infante, J. R., Ansell, S. M., Nemunaitis, J. J., Weiss, G. R., Villalobos, V. M., Sikic, B. I., Taylor, M. H., Northfelt, D. W., and Carson, W. E. (2017) Safety and activity of varlilumab, a novel and first-in-class agonist anti-CD27 antibody, in patients with advanced solid tumors. *J. Clin. Oncol.* **35**, 2028–2036
26. Ansell, S. M., Flinn, I., Taylor, M. H., Sikic, B. I., Brody, J., Nemunaitis, J., Feldman, A., Hawthorne, T. R., Rawls, T., and Keler, T. (2020) Safety and activity of varlilumab, a novel and first-in-class agonist anti-CD27 antibody, for hematologic malignancies. *Blood Adv.* **4**, 1917–1926
27. Shapira-Frommer, R., van Dongen, M. G., Dobrenkov, K., Chartash, E., Liu, F., Li, C., Wnek, R., and Patel, M. (2020) O83 phase 1 study of an anti-CD27 agonist as monotherapy and in combination with pembrolizumab in patients with advanced solid tumors. *J. Immunother. Cancer*. https://doi.org/10.1136/LBA2019.3
28. Camerini, D., Walz, G., Loenen, W., Borst, J., and Seed, B. (1991) The T cell activation antigen CD27 is a member of the nerve growth factor/tumor necrosis factor receptor gene family. *J. Immunol.* **147**, 3165–3169
29. Teplyakov, A., Obmolova, G., Malia, T. J., and Gilliland, G. L. (2017) Crystal structure of CD27 in complex with a neutralizing noncompeting antibody. *Acta Crystallogr. F Struct. Biol. Commun.* **73**, 294–299
30. Jin, T., Guo, F., Kim, S., Howard, A., and Zhang, Y. Z. (2007) X-ray crystal structure of TNF ligand family member TL1A at 2.1A. *Biochem. Biophys. Res. Commun.* **364**, 1–6
31. Baeyens, K. J., De Bondt, H. L., Raeymaekers, A., Fiers, W., and De Ranter, C. J. (1999) The structure of mouse tumour-necrosis factor at 1.4 A resolution: Towards modulation of its selectivity and trimerization. *Acta Crystallogr. D Biol. Crystallogr.* **55**, 772–778
32. He, M. M., Smith, A. S., Oslob, J. D., Flanagan, W. M., Braisted, A. C., Whitty, A., Cancilla, M. T., Wang, J., Lugovskoy, A. A., and Yoburn, J. C. (2005) Small-molecule inhibition of TNF-α. *Science* **310**, 1022–1025
33. Wyzgol, A., Müller, N., Fick, A., Munkel, S., Grigoleit, G. U., Pfizenmaier, K., and Wajant, H. (2009) Trimer stabilization, oligomerization, and antibody-mediated cell surface immobilization improve the activity of soluble trimers of CD27L, CD40L, 41BBL, and glucocorticoid-induced TNF receptor ligand. *J. Immunol.* **183**, 1851–1861
34. Compaan, D. M., and Hymowitz, S. G. (2006) The crystal structure of the costimulatory OX40-OX40L complex. *Structure* **14**, 1321–1330
35. Zhan, C., Patskovsky, Y., Yan, Q., Li, Z., Ramagopal, U., Cheng, H., Brenowitz, M., Hui, X., Nathenson, S. G., and Almo, S. C. (2011) Decoy strategies: The structure of TL1A: DcR3 complex. *Structure* **19**, 162–171
36. Liu, W., Ramagopal, U., Cheng, H., Bonanno, J. B., Toro, R., Bhosle, R., Zhan, C., and Almo, S. C. (2016) Crystal structure of the complex of human FasL and its decoy receptor DcR3. *Structure* **24**, 2016–2023
37. Liu, W., Zhan, C., Cheng, H., Kumar, P. R., Bonanno, J. B., Nathenson, S. G., and Almo, S. C. (2014) Mechanistic basis for functional promiscuity in the TNF and TNF receptor superfamilies: Structure of the LIGHT: DcR3 assembly. *Structure* **22**, 1252–1262
38. Eck, M. J., and Sprang, S. R. (1989) The structure of tumor necrosis factor-alpha at 2.6 A resolution. Implications for receptor binding. *J. Biol. Chem.* **264**, 17595–17605
39. Sudhamsu, J., Yin, J., Chiang, E. Y., Starovasnik, M. A., Grogan, J. L., and Hymowitz, S. G. (2013) Dimerization of LTβR by LTα1β2 is necessary and sufficient for signal transduction. *Proc. Natl. Acad. Sci. U. S. A.* **110**, 19896–19901
40. Bodmer, J.-L., Schneider, P., and Tschopp, J. (2002) The molecular architecture of the TNF superfamily. *Trends Biochem. Sci.* **27**, 19–26
41. Schuepbach-Mallepell, S., Das, D., Willen, L., Vigolo, M., Tardivel, A., Lebon, L., Kowalczyk-Quintas, C., Nys, J., Smulski, C., and Zheng, T. S. (2015) Stoichiometry of heteromeric BAFF and APRIL cytokines dictates their receptor binding and signaling properties. *J. Biol. Chem.* **290**, 16330–16342
42. Oren, D. A., Li, Y., Volovik, Y., Morris, T. S., Dharia, C., Das, K., Galperina, O., Gentz, R., and Arnold, E. (2002) Structural basis of BLyS receptor recognition. *Nat. Struct. Biol.* **9**, 288–292
43. Hymowitz, S. G., Compaan, D. M., Yan, M., Wallweber, H. J., Dixit, V. M., Starovasnik, M. A., and de Vos, A. M. (2003) The crystal structures of EDA-A1 and EDA-A2: Splice variants with distinct receptor specificity. *Structure* **11**, 1513–1520
44. Chattopadhyay, K., Ramagopal, U. A., Mukhopadhaya, A., Malashkevich, V. N., DiLorenzo, T. P., Brenowitz, M., Nathenson, S. G., and Almo, S. C. (2007) Assembly and structural properties of glucocorticoid-induced TNF receptor ligand: Implications for function. *Proc. Natl. Acad. Sci. U. S. A.* **104**, 19452–19457

45. Bitra, A., Doukov, T., Croft, M., and Zajonc, D. M. (2018) Crystal structures of the human 4-1BB receptor bound to its ligand 4-1BBL reveal covalent receptor dimerization as a potential signaling amplifier. *J. Biol. Chem.* **293**, 9958–9969
46. Chin, S. M., Kimberlin, C. R., Roe-Zurz, Z., Zhang, P., Xu, A., Liao-Chan, S., Sen, D., Nager, A. R., Oakdale, N. S., and Brown, C. (2018) Structure of the 4-1BB/4-1BBL complex and distinct binding and functional properties of utomilumab and urelumab. *Nat. Commun.* **9**, 1–13
47. Wang, F., Chau, B., West, S. M., Kimberlin, C. R., Cao, F., Schwarz, F., Aguilar, B., Han, M., Morishige, W., and Bee, C. (2021) Structures of mouse and human GITR–GITRL complexes reveal unique TNF superfamily interactions. *Nat. Commun.* **12**, 1–9
48. Obmolova, G., Teplyakov, A., Malia, T. J., Wunderler, N., Kwok, D., Barone, L., Sweet, R., Ort, T., Scully, M., and Gilliland, G. L. (2017) Epitope-dependent mechanisms of CD27 neutralization revealed by X-ray crystallography. *Mol. Immunol.* **83**, 92–99
49. Silence, K., Dreier, T., Moshir, M., Ulrichts, P., Gabriels, S. M., Saunders, M., Wajant, H., Brouckaert, P., Huyghe, L., Van Hauwermeiren, T., Thibault, A., and De Haard, H. J. (2014) ARGX-110, a highly potent antibody targeting CD70, eliminates tumors via both enhanced ADCC and immune checkpoint blockade. *mAbs* **6**, 523–532
50. Silence, K., Ulrichts, P., De Haard, J. J. W., Dreier, T., Saunders, M. J. S., Wajant, H., Gabriels, S. M. E., and Moshir, M. (2019) *Antibodies to cd70*. Google Patents
51. Salzer, E., Daschkey, S., Choo, S., Gombert, M., Santos-Valente, E., Ginzel, S., Schwendinger, M., Haas, O. A., Fritsch, G., Pickl, W. F., Forster-Waldl, E., Borkhardt, A., Boztug, K., Bienemann, K., and Seidel, M. G. (2013) Combined immunodeficiency with life-threatening EBV-associated lymphoproliferative disorder in patients lacking functional CD27. *Haematologica* **98**, 473–478
52. Ota, T., Suzuki, Y., Nishikawa, T., Otsuki, T., Sugiyama, T., Irie, R., Wakamatsu, A., Hayashi, K., Sato, H., Nagai, K., Kimura, K., Makita, H., Sekine, M., Obayashi, M., Nishi, T., *et al.* (2004) Complete sequencing and characterization of 21,243 full-length human cDNAs. *Nat. Genet.* **36**, 40–45
53. Goodwin, R. G., Alderson, M. R., Smith, C. A., Armitage, R. J., VandenBos, T., Jerzy, R., Tough, T. W., Schoenborn, M. A., Davis-Smith, T., Hennen, K., Falk, B., Cosman, D., Baker, E., Sutherland, G., Grabstein, K., *et al.* (1993) Molecular and biological characterization of a ligand for CD27 defines a new family of cytokines with homology to tumor necrosis factor. *Cell* **73**, 447–456
54. Ghosh, S., Kostel Bal, S., Edwards, E. S. J., Pillay, B., Jimenez Heredia, R., Erol Cipe, F., Rao, G., Salzer, E., Zoghi, S., Abolhassani, H., Momen, T., Gostick, E., Price, D. A., Zhang, Y., Oler, A. J., *et al.* (2020) Extended clinical and immunological phenotype and transplant outcome in CD27 and CD70 deficiency. *Blood* **136**, 2638–2655
55. Chang, V. T., Crispin, M., Aricescu, A. R., Harvey, D. J., Nettleship, J. E., Fennelly, J. A., Yu, C., Boles, K. S., Evans, E. J., and Stuart, D. I. (2007) Glycoprotein structural genomics: Solving the glycosylation problem. *Structure* **15**, 267–273
56. Vonrhein, C., Flensburg, C., Keller, P., Sharff, A., Smart, O., Paciorek, W., Womack, T., and Bricogne, G. (2011) Data processing and analysis with the autoPROC toolbox. *Acta Crystallogr. D Biol. Crystallogr.* **67**, 293–302
57. Waterhouse, A., Bertoni, M., Bienert, S., Studer, G., Tauriello, G., Gumienny, R., Heer, F. T., de Beer, T. A. P., Rempfer, C., Bordoli, L., Lepore, R., and Schwede, T. (2018) SWISS-MODEL: Homology modelling of protein structures and complexes. *Nucleic Acids Res.* **46**, W296–W303
58. Adams, P. D., Afonine, P. V., Bunkoczi, G., Chen, V. B., Davis, I. W., Echols, N., Headd, J. J., Hung, L. W., Kapral, G. J., Grosse-Kunstleve, R. W., McCoy, A. J., Moriarty, N. W., Oeffner, R., Read, R. J., Richardson, D. C., *et al.* (2010) PHENIX: A comprehensive Python-based system for macromolecular structure solution. *Acta Crystallogr. D Biol. Crystallogr.* **66**, 213–221
59. Emsley, P., Lohkamp, B., Scott, W. G., and Cowtan, K. (2010) Features and development of Coot. *Acta Crystallogr. D Biol. Crystallogr.* **66**, 486–501